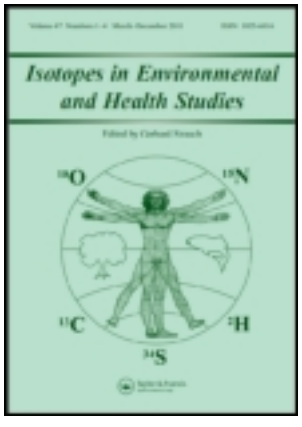

Isotopes in Environmental and Health Studies

Publication details, including instructions for authors and subscription information:
http://www.tandfonline.com/loi/gieh20

Early Aptian carbon and sulphur isotope signatures at ODP Site 765

Nicole DeBond [a], Rosie L. Oakes [b], Adina Paytan [c] & Ulrich G. Wortmann [b]

[a] Department of Earth Sciences, Memorial University of Newfoundland, St John's, NL, Canada

[b] Department of Geology, University of Toronto, Toronto, ON, Canada

[c] Institute of Marine Sciences, University of California Santa Cruz, Santa Cruz, CA, USA

Available online: 22 Feb 2012

To cite this article: Nicole DeBond, Rosie L. Oakes, Adina Paytan & Ulrich G. Wortmann (2012): Early Aptian carbon and sulphur isotope signatures at ODP Site 765, Isotopes in Environmental and Health Studies, 48:1, 180-194

To link to this article: http://dx.doi.org/10.1080/10256016.2012.659732

Isotopes in Environmental and Health Studies
Vol. 48, No. 1, March 2012, 180–194

Taylor & Francis
Taylor & Francis Group

Early Aptian carbon and sulphur isotope signatures at ODP Site 765

Nicole DeBond[a]*, Rosie L. Oakes[b], Adina Paytan[c] and Ulrich G. Wortmann[b]

[a]*Department of Earth Sciences, Memorial University of Newfoundland, St John's, NL, Canada;* [b]*Department of Geology, University of Toronto, Toronto, ON, Canada;* [c]*Institute of Marine Sciences, University of California Santa Cruz, Santa Cruz, CA, USA*

(*Received 30 June 2011; final version received 16 January 2012*)

Current carbon and sulphur isotope ratios ($\delta^{13}C$ and $\delta^{34}S$) suggest there were major shifts in partitioning between reduced and oxidised reservoirs of carbon and sulphur during the Early Cretaceous. However, the $\delta^{13}C$ and $\delta^{34}S$ records are composed from different Ocean Drilling Program sites and are hard to correlate at high resolution. We present high-resolution Aptian $\delta^{13}C_{org}$ and $\delta^{34}S_{barite}$ values derived from the same set of samples, enabling a higher certainty correlation than previously possible. Two major hypotheses aim to explain the Early Aptian S-isotope excursion: increased volcanic degassing and/or fluctuations in the marine sulphate concentration. Our S-isotope data provide tight constraints on the timing and magnitude of volcanic flux required. We show that the observed S-isotope signature can be explained by a 2 Ma pulse of increased volcanic flux, injecting $\sim 4.5 \times 10^{18}$ mol C into the atmosphere. Further work is needed to evaluate whether these fluxes are compatible with the existing C-isotope record.

Keywords: barite; carbon-13; Cretaceous age; Early Cretaceous; isotope geochemistry; ocean anoxic event, ocean drilling programme (ODP); oxygen-18; sulphur-34

1. Introduction

The microbially mediated reduction of sulphate (MSR) favours ^{32}S over ^{34}S, producing reduced sulphur compounds which are significantly enriched in ^{32}S. Heimo Nielsen was one of the pioneering scientists who used this relationship to deduce changes in weathering, hydrothermal fluxes and the burial fluxes of evaporites and sulphides [1]. Similarly, photosynthesis favours ^{12}C over ^{13}C, which allows us to track changes in the global carbon cycle. The geochemical cycles of carbon and sulphur are coupled through MSR. During MSR, organic matter (OM) is oxidised, while sulphate is reduced producing hydrogen sulphide (H_2S) that, given sufficient availability of iron, is buried as pyrite. In the contemporary ocean, MSR is usually limited by the availability of OM, rather than the availability of sulphate [2]. Under these conditions, pyrite and OM burial fluxes are positively related, as increasing OM deposition results in the production of more H_2S

*Corresponding author. Email: nicole.debond@mun.ca

ISSN 1025-6016 print/ISSN 1477-2639 online

http://dx.doi.org/10.1080/10256016.2012.659732
http://www.tandfonline.com

by MSR [2]. The isotopic signatures of sedimentary OM and pyrite are also positively correlated. Increasing the burial flux of OM increases the amount of ^{12}C removed from the ocean, resulting in a positive $\delta^{13}C$ shift in OM as the ocean becomes more enriched in ^{13}C [3]. Increasing the production of H_2S results in increasing pyrite burial, preferentially removing ^{32}S from the ocean, and causing a positive $\delta^{34}S$ shift in seawater sulphate [3].

During the Early Cretaceous, a pronounced negative shift in $\delta^{34}S_{barite}$ (which records seawater sulphate) co-occurs with a significant positive $\delta^{13}C$ excursion in the marine carbonate, marine OM and terrestrial records (Figure 1) [4–6]. Our ability to interpret the relationship between these records, however, is hampered by the vastly different residence times of carbon and sulphur in the ocean. The residence time of carbon in the ocean is orders of magnitude less than that for sulphate ($\sim$10–20 Ma, [3,7,8]); therefore, the $\delta^{13}C_{org}$ record is more sensitive and will respond much faster to short-term changes than the $\delta^{34}S_{barite}$ record. Furthermore, the exact timing of the respective perturbation in each of these records and their relation to each other are difficult to establish. This is because existing records are obtained from different localities, limiting the temporal resolution of the record and the ability to correlate among records to the biostratigraphic resolution of the respective sample sets.

We try to constrain the relationship between the Aptian $\delta^{13}C_{org}$ and $\delta^{34}S_{barite}$ records by measuring both isotope ratios from a single sample set. Furthermore, we aim to improve the temporal resolution of the $\delta^{34}S_{barite}$ record in order to explore whether a smaller sized marine sulphate reservoir at that time resulted in an increase in the variability of the $\delta^{34}S_{barite}$ signal [9,10]. This latter point is of particular interest, as fluid inclusion studies suggest that sulphate concentrations at that time were as low as 5–12 mM [10], and modelling studies suggest concentrations as low as 1 mM [9]. We also discuss ways to distinguish between barite samples that are impacted by post-burial alteration or processing artefacts and those that are likely to faithfully record seawater signatures. Finally, we explore whether changes to mantle degassing rates can explain the observed $\delta^{34}S_{barite}$ signature using a S-cycle model.

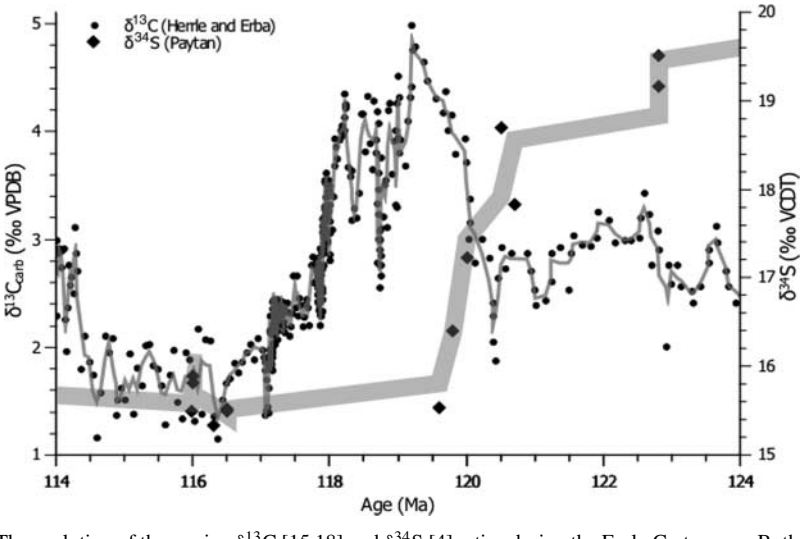

Figure 1. The evolution of the marine $\delta^{13}C$ [15,18] and $\delta^{34}S$ [4] ratios during the Early Cretaceous. Both signals show perturbations with respect to their steady-state values which reach a maximum at around 119 Ma. The C-isotope values increase, whereas the S-isotope values decrease, suggesting that the C and S redox cycles must have been decoupled during this perturbation. Note, however, that the vastly different marine residence times of C and S complicate a direct interpretation of these records (see [4,9] for discussion).

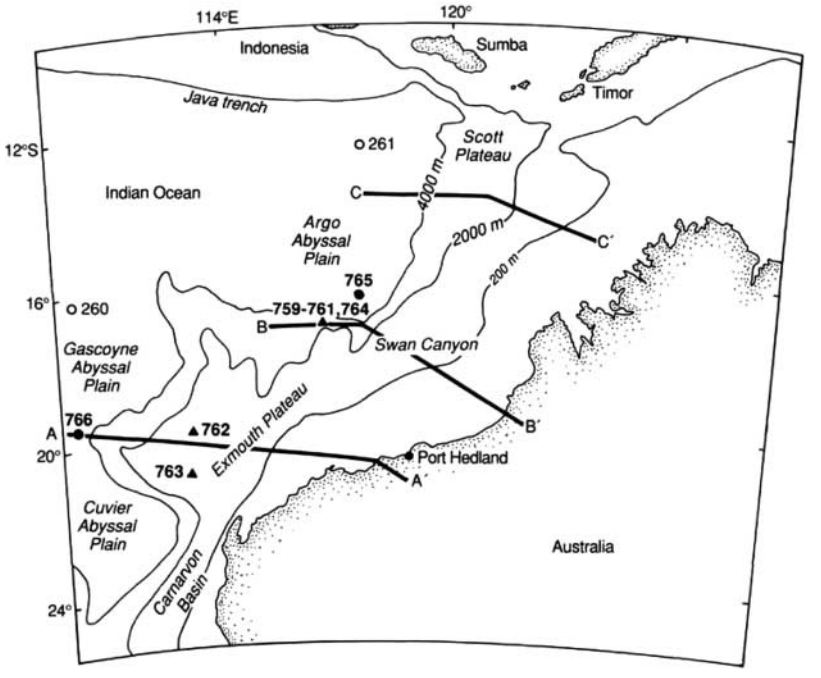

Figure 2. Bathymetry of north-western Australia including drill sites from ODP Leg 123 (closed circles) [11].

2. Methods

2.1. *Site selection*

Leg 123 of the Ocean Drilling Program (ODP) investigated the Argo and Gascoyne Abyssal plains in the northeast Indian Ocean, off the north-western margin of Australia in 1988 (Figure 2). Rifting along the northern and western margins of Australia created these plains during the Late Jurassic, forming the earliest parts of the Indian Ocean. A major objective for Leg 123 was to improve Mesozoic magneto-biostratigraphy and the geological timescale for the mid-(paleo)latitudes [11]. Although Site 765 is located relatively close to shore (within 75 km of the continental margin, at 15°58.54′ S 117°34.49′ E), the dry climate and low relief of north-western Australia resulted in sediment-starved conditions amenable to stratigraphic analyses [11]. Good core recovery and an established biostratigraphic framework for the Aptian at Site 765 suggest that a complete capture of the Aptian isotope excursions is possible. We selected 125 samples from Site 765, Core C in order to ensure capture of the Early Aptian C-isotope excursion as well as the Aptian Oceanic Anoxic Event (OAE1a).

2.2. *Sampling strategy*

Marine barite faithfully records the isotopic composition of marine sulphate [12]. Barite is continuously deposited on the seafloor and therefore does not suffer from temporal gaps that characterise the δ^{34}S record from evaporite minerals [4,13,14]. However, barite is susceptible to diagenetic dissolution once sulphate is depleted from the interstitial waters. We therefore focused only on core intervals with low total organic carbon (TOC) content as this makes them less favourable

for sulphate reduction. All samples were freeze-dried (−40 °C, 200 mbar), milled to a fine silt (∼0.02 mm) and subsequently divided for C and S isotope analyses.

We measured the $\delta^{13}C$ signal on bulk organic carbon which records the global $\delta^{13}C$ signal even when present in trace amounts [5,15]. After acidification to remove carbonates, TOC was determined using an elemental analyser (Eurovector EA3000). Calibrations were performed using an internal standard (atropine sulphate, $(C_{17}H_{23}NO_3)_2{\cdot}H_2SO_4$, 60.3% C). Multiple measurements of the standard indicated <5% relative error for TOC values. Stable carbon isotope ratios were determined on the de-calcified residue using a mass spectrometer (ThermoFinnigan MAT 253) in continuous flow mode via a Conflow III open split interface. Measurements were referenced relative to laboratory standard atropine ($C_{17}H_{23}NO_3$, −23.94‰ Vienna Pee Dee Belemnite (VPDB)), which was itself referenced against international standard NBS-22 (−29.7‰ VPDB). The accumulated error (1σ) for multiple measurements of the $\delta^{13}C$ value for atropine was 0.09‰ ($n = 56$).

After establishing the $\delta^{13}C_{org}$ record of the Early Aptian at Site 765, we selected a subset of 48 samples which represent the Aptian excursion for barite separation, purification and $\delta^{34}S_{barite}$ measurements. We followed the 8-day multi-step leaching procedure of Paytan [13], which produced a residue containing barite and a few other refractory minerals such as rutile [16]. We assessed the samples for purity and evidence of diagenesis using a scanning electron microscope SEM/EDS (JEOL, JSM-840, PGT/AAT EDS detector – thin window – IXRF 500 digital pulse processor). Almost half (23) of the samples contained enough barite for isotope analysis. These samples had low barite content (<10% barite) as expected from the continental proximity of the site. We purified the barite-bearing samples using a method based on Breit *et al*. [17]. In the presence of high concentrations of aqueous sodium carbonate, the sulphate in barite was replaced by carbonate, which produced barium carbonate and sulphate ions. We separated the sulphate ions via filtration (using 0.22 μm syringe filters), and acidified the solution to pH 2. We then added barium chloride in excess, which caused barite to precipitate. This process produced pure barite without affecting the S and O isotopes of the sulphate [17].

The purified barite was weighed (200 μg) into tin capsules, with an equal volume of vanadium pentoxide. $\delta^{34}S_{barite}$ was measured in duplicate using a Eurovector EA 3000 coupled to a ThermoFinnigan MAT 253 mass spectrometer in continuous flow mode via a Conflow III open split interface. We calibrated the $\delta^{34}S_{barite}$ results using international standards NBS-127 (21.1‰ Vienna Canyon Diablo Troilite (VCDT)), IAEA-SO-5 (0.49‰ VCDT) and IAEA-SO-6 (−34.05‰ VCDT). The accumulated errors (1σ) for repeated measurements of these standards were 0.11, 0.13 and 0.18‰, respectively ($n = 13$ for each).

For those samples with enough remaining material, we measured $\delta^{18}O_{barite}$ using the following procedure: Barite (135 μg) was added to Ag cups and pyrolysed at 1400°C over glassy carbon on a Hekatech HT-EA using helium as a carrier gas. The produced CO was routed through an Ascarite trap, separated on a Molsieve 5A, and subsequently measured on a ThermoFinnigan Mat 253 in continuous flow mode using the Conflo III open split interface. The system was calibrated using the international standards USGS-32 (25.7‰ Vienna Standard Mean Ocean Water (VSMOW)) and NBS-127 (9.3‰ VSMOW). Analytical reproducibility of the measurements was determined by running several replicates of an in-house standard ($BaSO_4$ with $\delta^{18}O = 12.38$‰) with each run. The accumulated error (1σ) of the in-house standard measured at the beginning, middle and end of each run from 12 individual runs (i.e. 3 per run = 36 total) was 0.26 ‰. All isotopic data are reported in the conventional delta notation with respect to VPDB, VCDT, or VSMOW as applicable.

The age-depth model for Site 765C is based on correlation with a composite record of $\delta^{13}C_{carb}$ from [15,18]. Sample depths (in metres below sea floor) reported by the ODP for Site 765C were converted to age based on bio-, chemo-, and magnetostratigraphic correlation with this composite record (Figure 3). The top of the record was correlated using the NC7a-NC7b boundary as reported

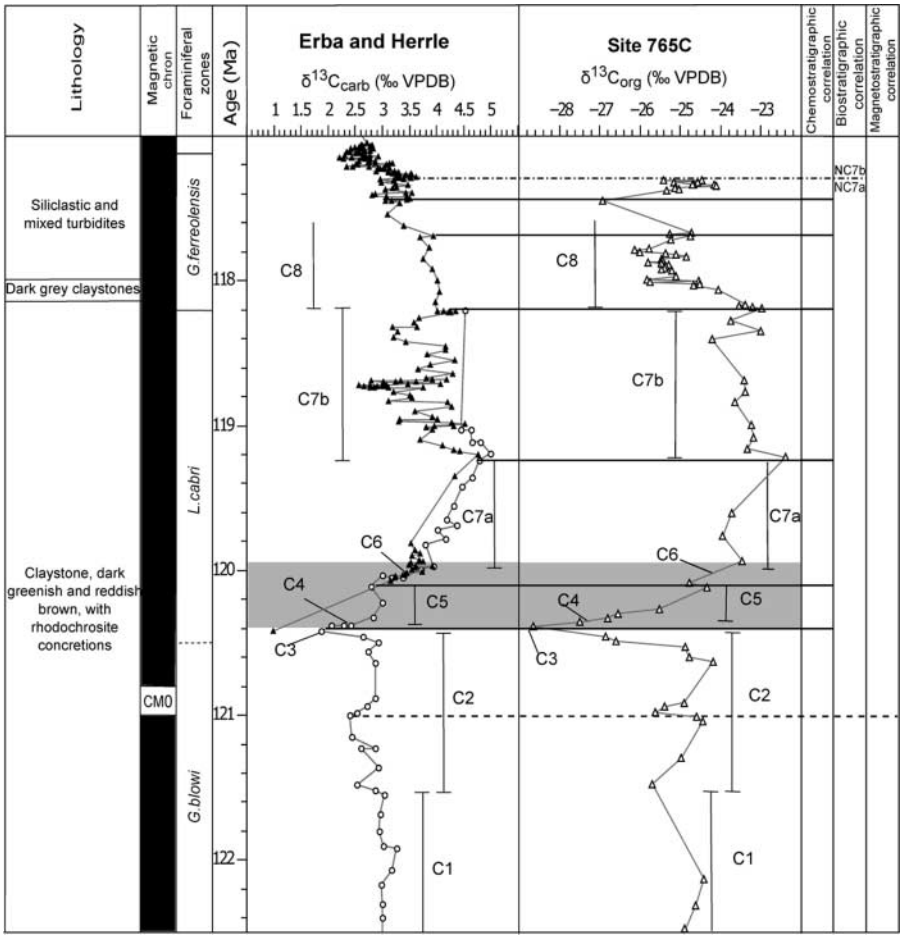

Figure 3. We correlate our $\delta^{13}C_{org}$ record from ODP Site 765C chemostratigraphically against a record that is biostratigraphically well defined [15,18]. The upper dashed tie line refers to the boundary between nanofossil zones NC7b/NC7a [19,20]. The lower dashed tie line refers to the base of magnetozone M0 [18,19]. The chemostratigraphic correlation is based on the C-zone stratigraphy proposed by Menegatti *et al.* [5], and ages are after Leckie *et al.* [21]. The location of OAE1a is determined by the C-zone stratigraphy in [5], and is marked by the grey bar. We map our data to absolute ages to provide a common reference frame between different sampling sites. Knowledge of absolute ages or the duration of biozones is not implied.

in [19,20]. The central portion of the record was correlated with [15,18] using isotopic excursions, made possible by the fact that $\delta^{13}C_{carb}$ and $\delta^{13}C_{org}$ record similar patterns during the Aptian OAE1a [5]. The base of the record was correlated using the base of the magnetic reversal CM0 as recorded in [18,19]. Note that Figure 3 does not imply knowledge of the duration of individual biozones or their absolute ages (which are revised frequently). We map our data to absolute ages because it provides a common reference frame between different sampling sites which are already mapped to the timescale published in [21].

2.3. *The $\delta^{34}S$ model*

To assist with data interpretation, we use a S-cycle model. The model consists of two parts: (A) a simple box model which describes the fluxes of S in and out of the ocean and (B) a model which describes the pyrite burial flux as a function of marine sulphate concentrations [9]. However,

unlike the model in [9], we do not explicitly compute the global pyrite burial flux, but rather describe it with the following parameterisation:

$$\mathrm{FB}_{\mathrm{Pyrite\_f}} = \mathrm{FB}_{\mathrm{Pyrite\_i}} * c/(1.8685 + c), \tag{1}$$

where $\mathrm{FB}_{\mathrm{Pyrite\_f}}$ denotes the resulting burial flux, $\mathrm{FB}_{\mathrm{Pyrite\_i}}$ denotes the initial burial flux, and c equals the marine sulphate (SO_4^{2-}) concentration in millimolar [9].

The sulphate concentration-dependent pyrite burial fluxes are then used as input parameters in a box model describing the evolution of the marine SO_4^{2-} concentration as

$$\frac{\partial[SO_4^{2-}]}{\partial t} = \mathrm{FW}_{\mathrm{pyrite}} + \mathrm{FW}_{\mathrm{VS}}(t) + \mathrm{FW}_{\mathrm{EV}} - (\mathrm{FB}_{\mathrm{Pyrite}}([SO_4^{2-}]) + \mathrm{FB}_{\mathrm{CaSO_4}}), \tag{2}$$

where $[SO_4^{2-}]$ denotes the amount of SO_4^{2-} in the ocean, $\mathrm{FW}_{\mathrm{Pyrite}}$ is the sulphur flux from pyrite weathering, $\mathrm{FW}_{\mathrm{VS}}$ is the sulphur flux from mantle degassing, $\mathrm{FW}_{\mathrm{EV}}$ is the evaporite weathering flux, $\mathrm{FB}_{\mathrm{Pyrite}}([SO_4^{2-}])$ is the pyrite burial flux as a function of the marine SO_4^{2-} concentration (see Equation (1)), and $\mathrm{FB}_{\mathrm{CaSO_4}}$ is the evaporitic burial flux. We force the model by varying the volcanic flux $\mathrm{FW}_{\mathrm{VS}}$ through time. Similar equations can be written for the fluxes of ^{32}S and ^{34}S, and their concentrations depending on the respective $\delta^{34}S$ values in order to calculate the marine $\delta^{34}S_{\mathrm{sulphate}}$.

We adjust all fluxes to achieve steady state under conditions which approximate modern conditions, but we do not strive to match them exactly. Assuming an ocean volume of $1.38 \times 10^{18}\ m^3$ [22], our model reaches steady-state conditions for a sulphate concentration of 27 mM, a pyrite weathering flux of $0.55 \times 10^{12}\ mol\ a^{-1}$, a volcanic flux of $0.5 \times 10^{12}\ mol\ a^{-1}$, an evaporite weathering flux of $0.95 \times 10^{12}\ mol\ a^{-1}$, a pyrite burial flux of $0.901 \times 10^{12}\ mol\ a^{-1}$, and an evaporite burial flux of $1.1 \times 10^{12}\ mol\ a^{-1}$. To achieve isotopic equilibrium, we assign the following isotopic ratios: volcanic input 0‰ (VCDT), evaporitic weathering 22‰ (VCDT), and pyrite weathering −17‰ (VCDT). We prescribe the isotopic offset between ocean water and pyrite as −36‰, and assume that $CaSO_4$ precipitates in isotopic equilibrium with ocean water. Using these parameters, our steady-state ocean attains a $\delta^{34}S_{\mathrm{sulphate}}$ ratio of 22‰ (VCDT), which is close to the Cenozoic long-term average [14]. All model runs are started at 130 Ma with an initial sulphate concentration of 8 mM (see [9] for discussion), and are only forced with variations in the volcanic input flux.

3. Results and discussion

3.1. *Carbon isotopes*

The $\delta^{13}C_{\mathrm{org}}$ isotope data from Site 765 reproduces the major features of the Aptian C-isotope excursion (Figure 3). Specifically the negative spike immediately preceding OAE1a, as well as the subsequent positive excursion are well represented. However, while developing our age–depth model, we noticed that the chemostratigraphic C-zone stratigraphy proposed by Menegatti *et al*. [5] does not fully represent the $\delta^{13}C_{\mathrm{carb}}$ record from [15] or the $\delta^{13}C_{\mathrm{org}}$ record from this study. We therefore propose that the C7 zone is split into C7a and C7b (Figure 3). Zone C7a represents the steady build up to maximum $\delta^{13}C$ values of 4.7‰ [15] and 5.0‰ [18] which correlates with the Early Aptian positive $\delta^{13}C$ excursion [5]. Zone C7b represents a period of high $\delta^{13}C$ fluctuation, with $\delta^{13}C_{\mathrm{carb}}$ values shifting between 2.5 and 4.5‰ before coming to a peak at 4.3‰ [15]. This zone is not seen in the Cismon record published by Erba *et al*. [18] from which Menegatti *et al.* [5] established the C-zone stratigraphy. The subsequent drop in $\delta^{13}C$ represents the start of the C8 zone, the top of which is undefined due to unconformities in both sections studied in [5].

The negative spike preceding OAE1a is much more prominent in our C_{org}-derived data than in the carbonate-derived data in [15] (Figure 3). This is seen in other $\delta^{13}C_{org}$ data sets [5,23]; however, the reason for this offset remains unclear. There are two main theories put forth to explain this sharp negative spike: the catastrophic dissociation of gas hydrates, which would have released large volumes of very ^{13}C-depleted (∼–60‰) methane into the ocean (e.g. [9,24–26]), and/or extensive CO_2 outgassing associated with the emplacement of the Ontong Java and Manihiki plateaus introducing ^{13}C-depleted CO_2 into the ocean [27–30].

The negative spike is followed by a quick recovery which is concomitant with OAE1a [21] and a subsequent positive excursion of ∼2‰ between ∼120 and 118 Ma observed both in our $\delta^{13}C_{org}$ and in the $\delta^{13}C_{carb}$ record of [15], which is similar in magnitude to that observed at other Pacific sites [31,32]. The cause of the positive organic carbon isotope excursion is not entirely clear. It has been proposed that increased hydrothermal fluxes could provide otherwise biolimiting metals (e.g. Fe), resulting in increased productivity and a more pronounced transfer of C to the OM reservoir [33]. It has also been suggested that this excursion could be attributed to changes in the volcanic flux of CO_2 associated with the emplacement of the Ontong Java and Manihiki Plateaus. Widespread oceanic stratification, subsequent enhanced burial of organic C, and a negative Os isotopic excursion [34] are consequences of such an emplacement. Additionally, global warming associated with increases in CO_2 could cause changes in thermohaline circulation, increasing nutrient recycling and enhanced productivity [5]. Other authors hypothesise that anoxic conditions during OAE1a led to increased nutrient recycling [35] and a subsequent increase in the efficiency of the biological pump, ultimately resulting in enhanced burial of organic C [21,36]. Reduced sulphate availability could also cause increased OM burial via the inhibition of MSR [9]. Many of these ideas have been combined into a model describing OAE2a [37].

3.2. *Sulphur isotopes*

Figure 4 shows the relationship between the $\delta^{34}S_{barite}$ from this study and the $\delta^{34}S_{barite}$ published in [4]. The study by Paytan *et al.* [4] is a composite record from multiple ODP sites and covers a much longer timescale than this study, but in lower resolution. We allocated ±0.5 Ma error on each point from [4] as indicated by the grey envelope, because the age model used was based on low resolution biostratigraphy and strontium isotopes from [21,38]. The uncertainty in the correlation of this multi-core data set illustrates why it is important to compose a high-resolution $\delta^{13}C$ and $\delta^{34}S$ record from a single core.

One of our primary goals was to improve on the $\delta^{34}S_{barite}$ sample density during the Early Aptian C-isotope excursion. We were able to increase sample resolution during the peak of the positive $\delta^{13}C_{org}$ excursion (120–118 Ma), but failed to recover suitable samples during the negative $\delta^{13}C_{org}$ excursion occurring between 120.5 and 120 Ma (Figure 4, Table 1). Only 3 of the 10 samples chosen for barite extraction during the latter interval contained enough barite for analysis. There are several possible explanations for the low barite concentrations observed during this time interval: (A) Sediments which are time-equivalent with OAE1a directly overly the sediments which record the negative C_{org}-isotope spike. These sediments could have a higher TOC content, which may enhance sulphate reduction, causing the depletion of porewater sulphate and subsequent dissolution and loss of barite; (B) The negative $\delta^{13}C_{org}$ peak coincides with the lowest S-isotope values which, if we follow Wortmann and Chernyavsky [9], indicates marine sulphate concentrations as low as 1 mM. This would have two major consequences: (1) Barite precipitation would become more difficult and (2) marine productivity would be severely affected by a lack of phosphorus. This is because low sulphate concentrations limit OM remineralisation by sulphate-reducing bacteria, the processes that returns phosphorus to the ocean [9]. Both processes would dramatically affect the burial rate of barite, which additionally may be affected by diagenetic dissolution [12].

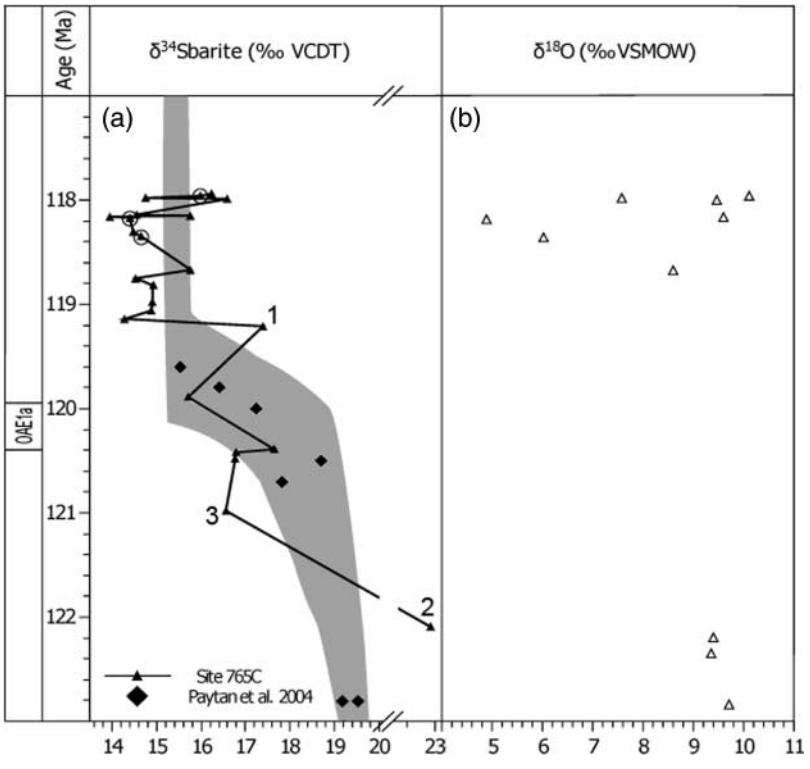

Figure 4. (a) The correlation between $\delta^{34}S_{barite}$ data from ODP Site 765C (triangles) versus the data set by Paytan *et al.* [4] (diamonds). The latter is a data set assembled from several ODP sites. The biostratigraphic records of the sites used in [4] reveal considerable uncertainty regarding the correlation of this data set with ODP Site 765C investigated here. We have thus assigned a ±0.5 Ma error to each point from [4] (see discussion in text) producing the uncertainty envelope shown in grey. Labelled points 1 and 2 are diagenetic barites, identified by high $\delta^{34}S_{barite}$ values and crystal morphology. Point 3 is likely marine barite (see discussion in text). (b) Sulphate-derived $\delta^{18}O$, which is highly sensitive to pyrite oxidation [40], from ODP Site 765C. Samples with anomalously low $\delta^{18}O_{barite}$ values have been circled in (a).

Our S-isotope data agree with the expected trends after accounting for three data points (labelled 1, 2, and 3 on Figure 4) which are discussed below. However, the samples falling between 119 and 118 Ma show much higher variability than observed in the lower resolution data set from [4]. It is possible that the new data indeed represent rapid changes in seawater sulphate isotopes. Alternatively, $\delta^{34}S_{barite}$ values may have been altered by diagenesis (e.g. [12,39]) and by oxidation of pyrite during the barite separation process because it was not performed under oxygen-free conditions [40]. Therefore, much care must be taken whilst interpreting these $\delta^{34}S_{barite}$ measurements. Marine barite can be distinguished from barite that is altered by diagenesis or produced by pyrite oxidation using crystal morphology and assessment of isotopic ratios ($\delta^{34}S_{barite}$ relative to surrounding samples and to $\delta^{18}O_{barite}$). In the following, we consider these factors for each barite sample recovered.

Two of our samples (1 and 2, Figure 4) show a positive offset of 2‰ or greater compared to the existing record from [4]. Such values are likely to be indicative of barite that precipitated in pore fluids from residual sulphate which was impacted by microbial reduction. Sulphate is liberated during the dissolution of primary barite and some of this sulphate is reduced by MSR resulting in ^{34}S-enriched residual sulphate relative to initial conditions. This enriched sulphate may reprecipitate to form diagenetic barite which is morphologically easy to identify [12]. Diagenetic barite crystals are 20–700 μm and tabular or platy in appearance (Figure 5) [12]. Inspection of

Table 1. Depth, age, TOC content (weight%), and C, S, and O isotopic composition of samples from Site 765C.

Identifier	Depth (mbsf)	Age (Ma)	$\delta^{13}C_{org}$ (‰ VPDB)	TOC (%)	$\delta^{34}S_{barite}$ (‰ VCDT)	$\delta^{18}O_{barite}$ (‰ VSMOW)
765C 34-R-1 099-100 cm	665.39	117.30	−24.66	0.74		
765C 34-R-2 049-050 cm	666.39	117.30	−25.60	0.73		
765C 34-R-3 099-100 cm	668.39	117.31	−24.75	0.74		
765C 34-R-4 036-040 cm	669.26	117.31	−25.33	0.81		
765C 35-R-1 096-100 cm	675.06	117.33	−24.85	0.13		
765C 35-R-2 047-050 cm	676.07	117.33	−24.89	0.17		
765C 35-R-2 146-150 cm	677.06	117.33	−24.35	1.04		
765C 35-R-3 053-054 cm	677.63	117.34	−24.29	2.05		
765C 36-R-1 099-100 cm	684.29	117.35	−25.30	0.70		
765C 36-R-2 099-100 cm	685.79	117.36	−25.20	0.70		
765C 36-R-6 009-010 cm	690.89	117.37	−25.52	0.71		
765C 36-R-6 054-057 cm	691.34	117.44	−27.07	0.69		
765C 37-R-1 099-100 cm	693.99	117.66	−24.91	0.72		
765C 37-R-2 050-051 cm	695.00	117.67	−25.44	0.10		
765C 37-R-3 052-053 cm	696.52	117.68	−24.94	0.07		
765C 37-R-3 099-100 cm	696.99	117.71	−25.41	0.11		
765C 38-R-1 099-100 cm	703.49	117.77	−25.93	0.09		
765C 38-R-2 049-050 cm	704.49	117.78	−26.29	0.07		
765C 38-R-2 147-150 cm	705.47	117.79	−26.17	0.08		
765C 38-R-3 099-100 cm	706.49	117.80	−25.53	0.08		
765C 38-R-4 044-046 cm	707.44	117.81	−25.29	0.10		
765C 38-R-4 145-146 cm	708.45	117.82	−25.03	0.07		
765C 38-R-5 099-100 cm	709.54	117.84	−25.63	0.11		
765C 38-R-6 045-047 cm	710.50	117.85	−25.61	0.14		
765C 38-R-6 147-149 cm	711.52	117.86	−25.65	0.09		
765C 38-R-7 062-063 cm	712.17	117.86	−25.97	0.08		
765C 39-R-1 099-100 cm	712.69	117.87	−25.64	0.13		
765C 39-R-2 049-050 cm	713.69	117.88	−25.45	0.14		
765C 39-R-2 149-150 cm	714.69	117.89	−25.55	0.11		
765C 39-R-3 099-100 cm	715.69	117.90	−25.56	0.10		
765C 39-R-4 087-089 cm	717.07	117.91	−25.64	0.11		
765C 39-R-5 015-016 cm	717.85	117.92	−25.39	0.14		
765C 40-R-1 099-100 cm	721.89	117.96	−25.28	0.11	16.24 ± 0.19	10.14
765C 40-R-2 054-055 cm	722.94	117.97			NR	
765C 40-R-2 149-150 cm	723.89	117.98	−25.99	0.07	15.98 ± 0.42	7.61
765C 40-R-3 099-100 cm	724.93	117.99	−24.72	0.22	NR	
765C 40-R-4 049-050 cm	725.97	118.00	−25.91	0.16	14.75 ± 1.05	9.52
765C 40-R-4 148-150 cm	726.96	118.01	−24.71	0.48	16.60 ± 1.59	
765C 40-R-5 059-060 cm	727.57	118.02	−24.85	0.15	NR	
765C 41-R-1 053-054 cm	730.93	118.05	−24.26	0.17	NR	
765C 42-R-1 099-100 cm	740.79	118.15	−23.58	0.10	14.55 ± 0.14	
765C 42-R-2 049-050 cm	741.79	118.16	−23.74	0.13	15.75 ± 0.21	9.63
765C 42-R-2 149-150 cm	742.79	118.17	−23.41	0.43	13.96 ± 0.15	
765C 42-R-3 099-100 cm	743.79	118.18	−23.20	0.18	14.40 ± 0.15	4.93
765C 42-R-4 049-050 cm	744.79	118.26	−23.95	0.11	NR	
765C 42-R-4 147-148 cm	745.77	118.33	−23.22	0.12	14.48 ± 0.12	
765C 42-R-5 059-060 cm	746.45	118.39	−24.41	0.16	14.66 ± 0.10	6.07
765C 43-R-1 099-100 cm	750.09	118.67	−23.61	0.05	15.77 ± 0.14	8.96
765C 43-R-2 049-050 cm	751.09	118.75	−23.59	0.15	14.54 ± 0.08	
765C 43-R-2 149-150 cm	752.09	118.82	−23.84	0.16	14.92 ± 0.06	
765C 43-R-4 049-050 cm	754.09	118.98	−23.45	0.16	14.91 ± 0.03	
765C 43-R-4 149-150 cm	755.09	119.06	−23.38	0.16	14.89 ± 0.27	
765C 43-R-5 099-100 cm	756.12	119.14	−23.53	0.16	14.29	
765C 43-R-6 049-050 cm	757.17	119.20	−22.61	0.17	17.40 ± 0.18[1]	
765C 44-R-1 099-100 cm	759.49	119.58	−23.92	0.31	NR	
765C 44-R-2 049-050 cm	760.49	119.74	−24.14	0.43	NR	
765C 44-R-3 002-003 cm	761.56	119.91	−23.66	0.26	15.71 ± 0.07	
765C 44-R-3 099-100 cm	762.53	120.06	−24.96	0.36	NR	
765C 44-R-4 049-050 cm	763.57	120.09	−24.52	0.25	NR	
765C 45-R-1 099-100 cm	769.19	120.24	−25.70	0.07	NR	

(*Continued*)

Table 1. Continued.

Identifier	Depth (mbsf)	Age (Ma)	$\delta^{13}C_{org}$ (‰ VPDB)	TOC (%)	$\delta^{34}S_{barite}$ (‰ VCDT)	$\delta^{18}O_{barite}$ (‰ VSMOW)
765C 45-R-2 048-050 cm	770.18	120.27	−26.71	0.08	NR	
765C 45-R-2 149-150 cm	771.19	120.30	−26.96	0.10	NR	
765C 45-R-3 099-100 cm	772.19	120.33	−27.63	0.18	17.64 ± 0.44	9.45
765C 45-R-4 084-085 cm	773.54	120.36	−28.78	0.54	16.78 ± 0.14	
765C 45-R-5 034-035 cm	774.58	120.43	−27.01	0.11	NR	
765C 45-R-5 134-135 cm	775.58	120.46	−26.74	0.26	NR	
765C 45-R-6 084-085 cm	776.61	120.50	−25.07	0.21	16.77 ± 0.33	9.39
765C 46-R-1 099-100 cm	778.79	120.57	−24.96	0.29	NR	
765C 46-R-2 049-050 cm	779.79	120.60	−24.38	0.13	NR	
765C 47-R-1 099-100 cm	788.39	120.88	−25.08	0.27	NR	
765C 47-R-2 049-050 cm	789.39	120.91	−25.56	0.27	NR	
765C 47-R-2 149-150 cm	790.39	120.95	−25.78	0.08	NR	
765C 47-R-3 099-100 cm	791.39	120.98	−24.77	0.22	16.56 ± 0.37[3]	9.74
765C 47-R-4 050-051 cm	792.40	121.01	−24.63	0.26	NR	
765C 47-R-4 149-150 cm	793.39	121.26	−25.15	0.78	NR	
765C 47-R-5 099-100 cm	794.39	121.44	−25.86	0.72	NR	
765C 48-R-1 099-100 cm	797.89	122.09	−24.60	0.28	22.91 ± 0.74[2]	
765C 48-R-2 049-050 cm	798.89	122.27	−24.80	0.22	NR	
765C 48-R-2 149-150 cm	799.89	122.46	−25.09	0.74	NR	
765C 48-R-3 099-100 cm	800.89	122.64	−25.11	0.71	NR	
765C 48-R-5 032-033 cm	803.22	123.08	−25.17	0.72		
765C 48-R-5 129-130 cm	804.19	123.26	−24.65	0.76		
765C 48-R-6 084-085 cm	805.24	123.45	−24.85	0.77		
765C 48-R-7 035-036 cm	806.25	123.64	−24.75	0.70		
765C 49-R-1 099-100 cm	807.29	123.83	−25.09	1.22		
765C 49-R-2 049-050 cm	808.29	124.01	−24.54	0.72		
765C 49-R-2 147-148 cm	809.27	124.19	−24.75	0.72		
765C 49-R-3 099-100 cm	810.29	124.38	−24.82	0.70		
765C 49-R-4 049-050 cm	811.29	124.57	−25.06	0.75		
765C 49-R-4 147-148 cm	812.27	124.75	−24.82	0.72		
765C 49-R-5 094-095 cm	813.24	124.93	−24.54	0.78		
765C 49-R-6 029-030 cm	813.79	125.03	−24.30	0.72		
765C 50-R-1 099-100 cm	816.59	125.55	−26.26	0.69		
765C 50-R-2 049-050 cm	817.59	125.73	−25.64	0.69		
765C 50-R-2 147-148 cm	818.57	125.92	−26.08	0.68		
765C 50-R-3 099-100 cm	819.59	126.10	−25.21	0.08		
765C 50-R-4 099-100 cm	821.09	126.38	−25.96	0.07		
765C 50-R-4 149-150 cm	821.59	126.47	−25.53	0.12		
765C 50-R-5 107-108 cm	822.67	126.67	−24.96	0.21		
765C 50-R-6 049-050 cm	823.59	126.84	−25.01	0.25		
765C 51-R-1 099-100 cm	825.99	127.29	−25.16	0.25		
765C 51-R-2 049-050 cm	826.99	127.47	−25.19	0.25		
765C 51-R-2 148-149 cm	827.98	127.66	−25.46	0.25		
765C 51-R-3 099-100 cm	828.99	127.84	−25.27	0.06		
765C 51-R-4 085-086 cm	830.35	128.09	−24.89	0.03		
765C 51-R-5 039-040 cm	831.39	128.29	−25.53	0.12		
765C 51-R-5 135-136 cm	832.35	128.46	−25.15	0.35		
765C 52-R-1 099-100 cm	835.49	129.05	−25.25	0.20		
765C 52-R-2 049-050 cm	836.49	129.23	−25.76	0.11		
765C 52-R-3 094-095 cm	838.44	129.59	−26.05	0.15		

Notes: Superscripts correspond to numbers identifying data points in Figure 4. Samples where no barite was recovered are marked as 'NR'.

scanning electron microscopy (SEM) micrographs verified that samples 1 and 2 shown in Figure 3 contain diagenetic barite.

Many of the samples falling between ∼119 and 118 Ma have lower $\delta^{34}S_{barite}$ values than expected from the curve of [4]. While it is possible that these lower values are representative of fast fluctuations in the seawater record, we did not separate our barites under oxygen-free

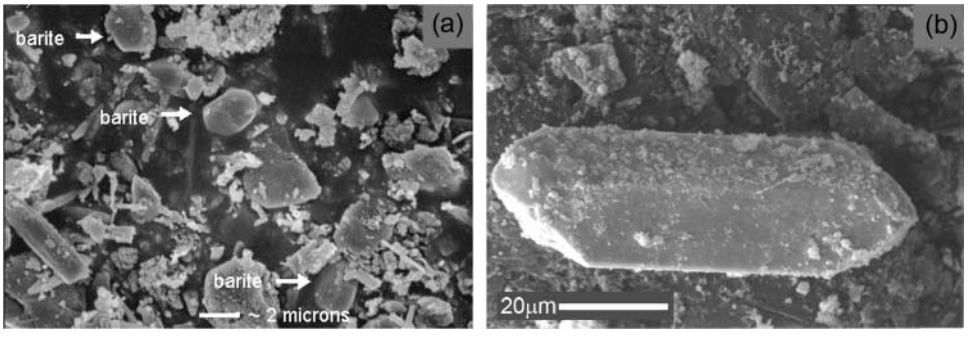

Figure 5. Diagenetic barite has a morphology that is distinct from marine barite [12]. Water column-derived barite (a), here in a sample that has ∼10% barite with contaminating phases such as rutile and silicates, is typically 5 μm, whereas diagenetic barite (b) is often tabular and ranges from 20 to 700 μm in length [12].

conditions. Therefore, there is a possibility that the integrity of their isotopic compositions is compromised, particularly if the samples are rich in pyrite. To assess this, we used $\delta^{18}O_{barite}$, which is a good indicator of contamination by pyrite oxidation. Sulphate that is produced by this process incorporates O from fresh water used in making the reagents, and is therefore more depleted in ^{18}O than seawater sulphate [40]. Sulphate produced during pyrite oxidation also tends to have low $\delta^{34}S$ due to the microbial preference for ^{32}S during MSR. Barite that contains sulphate produced from pyrite oxidation typically has low $\delta^{18}O_{barite}$ and low $\delta^{34}S_{barite}$ values.

We measured $\delta^{18}O_{barite}$ on 10 samples which had sufficient material, seven of which fall in the range of ∼119–118 Ma. Using the relationship between $\delta^{18}O_{barite}$ and $\delta^{34}S_{barite}$, we identify three samples (circled in Figure 4) that may include some barite produced from pyrite oxidation during the chemical separation, resulting in low $\delta^{18}O_{barite}$ (<8‰). Of the seven samples measured between ∼119 and 118 Ma, three had low $\delta^{18}O_{barite}$ and four did not. The samples with low $\delta^{18}O_{barite}$ lie off the curve of [4], while those with normal $\delta^{18}O_{barite}$ agree within analytical error with the previously published $\delta^{34}S$ curve. It appears that some of the observed variability in $\delta^{34}S_{barite}$ in this section of core could be attributed to pyrite oxidation during the barite separation procedure. Our data illustrate that $\delta^{34}S_{barite}$ performed on barite samples separated in the presence of oxygen, particularly when pyrite is present in the samples, should also be analysed for $\delta^{18}O_{barite}$ to test for processing artefacts.

The sample at ∼121 Ma (3, Figure 4) has a low $\delta^{34}S$ value relative to the existing fit [4]; however, it does not have a correspondingly low $\delta^{18}O_{barite}$ value indicative of contamination via pyrite oxidation. Inspection of SEM micrographs reveals no evidence of diagenetic barite. This suggests that this sample records an original seawater sulphate isotope ratio and that there were small-scale rapid fluctuations in the $\delta^{34}S_{barite}$ record during this time interval which were not previously captured and reported in [4] due to coarse sampling resolution.

3.3. *Implications for the Aptian C and S cycles*

Our data show that the Aptian sulphur and carbon cycle perturbations indeed occur at the same time, supporting the notion that they might be causally related. In fact, both geochemical cycles are tightly coupled through MSR which affects OM remineralisation [2]. That is, if we assume, e.g. increasing pyrite burial rates, we must also account for increased OM burial rates, and vice versa. As both reduced carbon and reduced sulphur are isotopically light relative to their oxidised forms (about −28‰ for C [41] and up to −70‰ for S [42]), changes in burial rates must result in positively coupled changes of their respective isotopic signatures. This coupling provides an important constraint on our interpretation, as the observed inverse relation of the isotope records

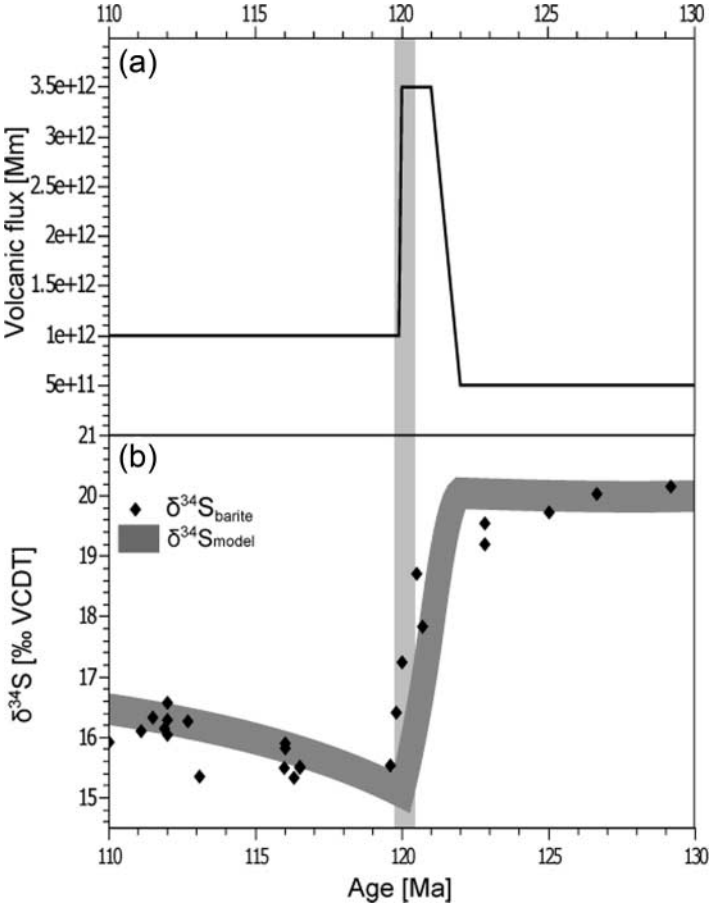

Figure 6. (a) Volcanic flux forcing function used in our sulphur cycle model. All ages after the timescale from [21]. (b) Comparison between the model and data from [4], assuming a sevenfold increase in the mantle degassing rate. The grey bar marks OAE1a.

requires a mechanism to decouple these signals. At present, three different scenarios have been proposed to explain the trends: (A) relocation of bulk OM burial from marine environments to terrestrial swamps [43]; (B) removal of sulphate from the Early Aptian ocean via evaporite systems [9]; (C) changes in the mantle degassing rates of C and S [4,27–30]. There is little evidence for scenario A, and scenario B has been explored extensively in [9]. Here, we explore the third possibility: whether changes to the mantle degassing rates can explain the observed S-isotope signature.

We model the S-cycle similar to Wortmann and Chernyavsky [9], with the exception that we force the model with the volcanic flux (Figure 6), instead of prescribing the evaporite precipitation rate. However, similar to Wortmann and Chernyavsky [9], we allow the pyrite burial rate to change as a function of marine sulphate concentration. The model is calibrated so that it achieves steady state under modern, pre-industrial conditions. We then vary the amplitude and timing of the volcanic input flux until we achieve a reasonable fit between model and data (Figure 6).

Currently, S-isotope modelling cannot determine whether the Early Aptian S-isotope excursion was caused by changes in the marine sulphate reservoir [9], or by changes to the volcanic degassing rate. However, our results provide constraints on the timing and magnitude of the

CO_2 added to the C-cycle, assuming that the volcanic fluxes for C and S change proportionally. Specifically, the volcanic CO_2 flux must have increased sevenfold between 122 and 120 Ma, adding a total of 4.5×10^{18} mol C in addition to the steady-state input during this time interval. Such an increase compares favourably to volcanic flux estimates based on Os-isotope measurements which record two major volcanic periods: one during OAE1a and one predating OAE1a [34]. For comparison, this is about 20 times more than the amount of carbon injected during the Paleocene/Eocene thermal maximum (PETM) [44]. This would have had considerable effects on the alkalinity budget of the ocean, plankton ecology, and the burial fluxes of organic and inorganic carbon.

Increased input fluxes must ultimately result in increased output fluxes. The burial fluxes for C and S are positively coupled; increased OM burial (resulting in a positive C-isotope excursion) must result in increased pyrite burial and, as such, in a positive S-isotope excursion. We did not model this case as a full-scale carbon cycle model, which could provide reasonable estimates of the variations in OM burial, is beyond the scope of this paper. However, the coupling of the C and S burial fluxes suggests that modelling the negative perturbations in the C and S isotope records by order of magnitude variations of the mantle degassing flux will cause subsequent large-scale positive isotope excursions in both the C and S isotope records. Interestingly, while the expected positive $\delta^{13}C$ isotope excursion is observed, $\delta^{34}S_{barite}$ values recover to near pre-perturbation values but do not become more positive [4].

4. Conclusions

The $\delta^{13}C_{org}$ and $\delta^{34}S_{barite}$ records indicate major perturbations in Earth's biogeochemical cycles during the Early Aptian, although, the mechanisms behind these perturbations remain controversial. We show that the $\delta^{13}C_{org}$ and $\delta^{34}S_{barite}$ excursions in the Aptian have a strong temporal relation, which supports the notion by Wortmann and Chernyavsky [9] that they might be causally related. We present new $\delta^{34}S_{barite}$ data between 119 and 118 Ma. However, interpreting sulphur isotope ratios obtained from barite can be difficult and much care is required when doing so. At present, it appears that between 119 and 118 Ma at least three of our samples are affected by pyrite oxidation during the barite separation process; however, at least four samples during that interval reflect an oceanographic signal. Further work is needed to make this distinction for samples that lack $\delta^{18}O_{barite}$ measurements.

Modelling shows that the S-isotope excursion can be explained by either reduced marine sulphate concentrations [9], and/or by increased volcanic flux [4]. Based on our results, we are unable to distinguish among these scenarios; however, the S-isotope data provide new constraints to model the volcanic outgassing hypothesis. We show that the S-isotope data can be explained by an order of magnitude change to the volcanic degassing flux, which corresponds to the addition of 4.5×10^{18} mol C within two million years. This is about 20 times the amount of carbon injected during the PETM [44], and must have had considerable effects on marine ecology, ocean alkalinity, and the burial fluxes of carbon and sulphur. Further research is needed to constrain whether these fluxes are compatible with the existing $\delta^{13}C$ data.

Acknowledgements

We thank Hong Li, Laura Lee, and Ellen Gray for invaluable help in the laboratory. Discussions with Jens Herrle, Elisabetta Erba, Helmut Weissert, and Stefan Markovic helped to shape our ideas. ODP Legacy samples were provided by the Integrated Ocean Drilling Program (IODP). This work was supported by NSERC Undergraduate Student Research Awards to N.D., an NSERC Discovery Grant to U.G.W., and by NSF CAREER Grant OCE-0449732 to A.P. Reviews by Marlene Reuschel and an anonymous reviewer greatly improved the content and clarity of this manuscript.

References

[1] H. Nielsen, Schwefelisotope im marinen Kreislauf und das δS der früheren Meere, *Geol. Rundsch.* **55**, 160 (1966).
[2] R.A. Berner and R. Raiswell, Burial of Organic Carbon and Pyrite Sulphur in Sediments over Phanerozoic Time: A New Theory, *Geochim. Cosmochim. Acta* **47**, 855 (1983).
[3] S.T. Petsch and R.A. Berner, Coupling the Geochemical Cycles of C, P, Fe and S: The Effect on Atmospheric O_2 and the Isotopic Records of Carbon and Sulfur, *Am. J. Sci.* **268**, 246 (1998).
[4] A. Paytan, M. Kastner, D. Campbell, and M.H. Thiemens, Seawater Sulfur Isotope Fluctuations in the Cretaceous, *Science* **304**, 1663 (2004).
[5] A.P. Menegatti, H. Weissert, R.S. Brown, R.V. Tyson, P. Farrimond, A. Strasser, and M. Caron, High-Resolution δ^{13}C Stratigraphy Through the Early Aptian 'Livello Selli' of the Alpine Tethys, *Paleoceanography* **13**, 530 (1998).
[6] D.R. Grocke, S. Hesselbo, and H.C. Jenkyns, Carbon-Isotope Composition of Lower Cretaceous Fossil Wood: Ocean-Atmosphere Chemistry and Relation to Sea-Level Change, *Geology* **27**, 155 (1999).
[7] G.E. Claypool, W.T. Holser, I.R. Kaplan, H. Sakai, and I. Zak, The Age Curves of Sulfur and Oxygen Isotopes in Marine Sulfate and Their Mutual Interpretation, *Chem. Geol.* **28**, 199 (1980).
[8] J.C.G. Walker, Global Geochemical Cycles of Carbon, Sulfur and Oxygen, *Mar. Geol.* **70**, 159 (1986).
[9] U.G. Wortmann and B.M. Chernyavsky, Effect of Evaporite Deposition on Early Cretaceous Carbon and Sulphur Cycling, *Nature* **446**, 654 (2007).
[10] T.K. Lowenstein, M.N. Timofeeff, S.T. Brennan, L.A. Hardie, and R.V. Demicco, Oscillations in Phanerozoic Seawater Chemistry: Evidence from Fluid Inclusions, *Science* **294**, 1086 (2001).
[11] S.K. Stewart (ed.), *Proceedings of the Ocean Drilling Program Initial Reports* (Ocean Drilling Program, College Station, TX, 1990), Vol. 123, 850 pp.
[12] A. Paytan, S. Mearon, K. Cobb, and M. Kastner, Origin of Marine Barite Deposits: Sr and S Isotope Characterization, *Geology* **30**, 747 (2002).
[13] A. Paytan, *Marine Barite. A Recorder of Ocean Chemistry, Productivity, and Circulation*, Ph.D. thesis, University of California, San Diego, 1995.
[14] A. Paytan, M. Kastner, D. Campbell, and M.H. Thiemens, Sulfur Isotopic Composition of Cenozoic Seawater Sulfate, *Science* **282**, 1459 (1998).
[15] J.O. Herrle, P. Koßler, O. Friedrich, H. Erlenkeuser, and C. Hemblen, High-Resolution Carbon Isotope Stratigraphy of the Aptian to Lower Albian: A Tool for Reconstructing Paleoceanography Changes and Paleobiological Evolution, *Earth Planet. Sci. Lett.* **218**, 149 (2004).
[16] A. Paytan and E.M. Griffith, Marine Barite: Recorder of Variations in Ocean Export Productivity, *Deep Sea Res. Part II* **54**, 687 (2007).
[17] G.N. Breit, E.C. Simmons, and M.B. Goldhaber, Dissolution of Barite for the Analysis of Strontium Isotopes and Other Chemical and Isotopic Variations Using Aqueous Sodium Carbonate, *Chem. Geol.* (*Isot. Geosci. Sect.*) **52**, 333 (1985).
[18] E. Erba, J.E.T. Channell, M. Claps, C. Jones, R.L. Larson, B. Opdyke, I. Premoli Silva, A. Riva, G. Salvini, and S. Torricelli, Integrated Stratigraphy of the Cismon Apticore (Southern Alps, Italy); a 'Reference Section' for the Barremian–Aptian Interval at Low Latitudes, *J. Foraminifer. Res.* **29**, 371 (1999).
[19] J. Ludden, F.M. Gradstein, A.C. Adamson, P.O. Baumgartner, R. Beausillon, T. Bolmer, P.R. Bown, R. Brereton, R.T. Buffler, D. Castillo, J. Compton, J.A. Dumoulin, C.M. Griffiths, D. Haig, D. Heggie, A. Ishiwatari, M.A. Kaminski, K. Kodama, D.C. Kopaska-Merkel, J.P. Marcoux, A. McMinn, M.J. Moran, J. Mutterlose, J.Q. Ogg, B. O'Neill, T. Plank, M. Riggins, M. Schott, G. Simmons, J. Thurow, A.C. Adamson, A.C. Adamson, and A. Palmer Julson, Shipboard Scientific Party, 1990. Site 765, in *Proceedings of the Ocean Drilling Program Initial Reports*, edited by S.K. Stewart (Ocean Drilling Program, College Station, TX, 1990), Vol. 123, pp. 63–267.
[20] J.O. Herrle and J. Mutterlose, Calcareous Nannofossils from the Aptian–Lower Albian of Southeast France: Palaeoecological and Biostratigraphic Implications, *Cretaceous Res.* **24**, 1 (2003).
[21] R.M. Leckie, T.J. Bralower, and R. Cashman, Oceanic Anoxic Events and Plankton Evolution: Biotic Response to Tectonic Forcing During the Mid-Cretaceous, *Paleoceanography* **17**, 1 (2002).
[22] K. Burke and C. Şengör, Ten Metre Global Sea-Level Change Associated with South Atlantic Aptian Salt Deposition, *Mar. Geol.* **83**, 309 (1988).
[23] U.G. Wortmann, J.O. Herrle, and H. Weissert, Altered Carbon Cycling and Coupled Changes in Early Cretaceous Weathering Patterns: Evidence from Integrated Carbon Isotope and Sandstone Records of the Western Tethys, *Earth Planet. Sci. Lett.* **220**, 69 (2004).
[24] B. Opdyke, E. Erba, R.L. Larson, and T. Herbert, Hot LIPs, Methane and the Carbon History of the Apticore, *J. Conf. Abs.* **6**, 203 (2001).
[25] D.J. Beerling, M.R. Lomas, and D.R. Grocke, On the Nature of Methane Gas-Hydrate Dissociation during the Toarcian and Aptian Oceanic Anoxic Events, *Am. J. Sci.* **302**, 28 (2002).
[26] A.H. Jahren, N.C. Arens, G. Sarmiento, J. Guerrero, and R. Amundson, Terrestrial Record of Methane Hydrate Dissociation in the Early Cretaceous, *Geology* **29**, 1159 (2001).
[27] M.A. Arthur, W.E. Dean, and S.O. Schlanger, in *The Carbon Cycle and Atmospheric CO_2: Natural Variations Archean to Present*, edited by E.T. Sundquist and W.E. Broecker (American Geophysical Union, Washington, DC, 1985), pp. 504–530.
[28] M.A. Arthur, H.C. Jenkyns, H.J. Brumsack, and S.O. Schlanger, in *Cretaceous Resources, Events, and Rhythms: Background and Plans for Research*, edited by R.N. Ginsburg and B. Beaudoin (Kluwer Academic Publishers, Norwell, MA, 1990), pp. 75–119.

[29] H. Weissert and E. Erba, Volcanism, CO_2 and Palaeoclimate: A Late Jurassic–Early Cretaceous Carbon and Oxygen Isotope Record, *J. Geol. Soc. London* **161**, 695 (2004).
[30] S. Méhay, C.E. Keller, S.M. Bernasconi, H. Weissert, E. Erba, C. Bottini, and P.A. Hochuli, A Volcanic CO_2 Pulse Triggered the Cretaceous Oceanic Anoxic Event 1a and a Biocalcification Crisis, *Geology* **37**, 819 (2009).
[31] M. Dumitrescu and S.C. Brassell, Compositional and Isotopic Characteristics of Organic Matter for the Early Aptian Oceanic Anoxic Event at Shatsky Rise, ODP Leg 198, *Palaeogeogr. Palaeoclimatol. Palaeoecol.* **235**, 168 (2006).
[32] M.M.M. Kuypers, Y. van Breugal, S. Schouten, E. Erba, and J.S. Sinninghe Damste, N_2-Fixing Cyanobacteria Supplied Nutrient N for Cretaceous Oceanic Anoxic Events, *Geology* **32**, 853 (2004).
[33] R.L. Larson and E. Erba, Onset of the Mid-Cretaceous Greenhouse in the Barremian–Aptian: Igneous Events and the Biological, Sedimentary, and Geochemical Responses, *Paleoceanography* **14**, 663 (1999).
[34] M.L.G. Tejada, K. Suzuki, J. Juroda, R. Coccioni, J.J. Mahoney, N. Ohkouchi, T. Sakamoto, and Y. Tatsumi, Ontong Java Plateau Eruption as a Trigger for the Early Aptian Oceanic Anoxic Event, *Geology* **37**, 855 (2009).
[35] P. Van Cappellen and E.D. Ingall, Benthic Phosphorus Regeneration, Net Primary Production, and Ocean Anoxia: A Model of the Coupled Marine Biogeochemical Cycles of Carbon and Phosphorus, *Paleoceanography* **9**, 677 (1994).
[36] T.J. Bralower, M.A. Arthur, R.M. Leckie, W.V. Sliter, D.J. Allard, and S.O. Schlanger, Timing and Paleoceanography of Oceanic Dysoxia/Anoxia in the Late Barremian to Early Aptian (Early Cretaceous), *Palaios* **9**, 335 (1994).
[37] D.D. Adams, M.T. Hurtgen, and B.B. Sageman, Volcanic Triggering of a Biogeochemical Cascade during Oceanic Anoxic Event 2, *Nat. Geosci.* **3**, 201 (2010).
[38] T.J. Bralower, R.M. Leckie, W.V. Sliter, and H.R. Thierstein, in *Geochronology, Time Scales and Global Stratigraphic Correlation*, edited by W.A. Berggren, D.V. Kent, M.-P. Aubry, and J. Hardenbol (Society for Sedimentary Geology, Tulsa, OK, 1995), Vol. 54, pp. 65–80.
[39] M.T. Hurtgen, M.A. Arthur, and A.R. Prave, The Sulfur Isotope Composition of Carbonate-Associated Sulfate in Mesoproterozoic to Neoproterozoic Carbonates from Death Valley, California, *Spec. Pap. Geol. Soc. Am.* **379**, 177 (2004).
[40] P.J. Marenco, F.A. Corsetti, D.E. Hammond, A.J. Kaufman, and D.J. Bottjer, Oxdation of Pyrite During Extraction of Carbonate Associated Sulfate, *Chem. Geol.* **247**, 124 (2008).
[41] M.H. O'Leary, Carbon Isotope Fractionation in Plants, *Phytochemistry* **20**, 553 (1981).
[42] U.G. Wortmann, S.M. Bernasconi, and M.E. Böttcher, Hypersulfidic Deep Biosphere Indicates Extreme Sulfur Isotope Fractionation During Single-Step Microbial Sulfate Reduction, *Geology* **29**, 647 (2001).
[43] R. Raiswell and D.E. Canfield, Sources of Iron for Pyrite Formation in Marine Sediments, *Am. J. Sci.* **298**, 219 (1998).
[44] L.R. Kump, T.J. Bralower, and A. Ridgwell, Ocean Acidification in Deep Time, *Oceanography* **22**, 94 (2009).